SUPPORTING INFORMATION

Krishnamoorthy Sathiyan,[a] Totan Mondal,[a] Poulami Mukherjee,[a] Shanti Gopal Patra,[a] Itay Pitussi,[a] Haya Kornweitz,[a] Ronen Bar-Ziv*[b] and Tomer Zidki*[a]

a Department of Chemical Sciences, and the Centers for Radical Reactions and Materials Research, Ariel University, Ariel, 4077625 Israel.

b Department of Chemistry, Nuclear Research Center-Negev, Beer-Sheva, 84190 Israel.

* bronen@post.bgu.ac.il
* tomerzi@ariel.ac.il

Experimental section

Chemicals and materials

Hexaammonium heptamolybdate tetrahydrate ($(NH_4)_6Mo_7O_{24}\cdot 4H_2O$) was obtained from Loba Chemie. Thiourea (H_2NCSNH_2), Iron nitrate nonahydrate ($Fe(NO_3)_3\cdot 9H_2O$), Cobalt nitrate hexahydrate ($Co(NO_3)_2\cdot 6H_2O$), and 5 wt% Nafion were purchased from Alfa Aesar. All the chemicals were used as received without further purification. Millipore water (deionized water, DI) with >15 MΩ·cm resistivity is used throughout the experiments.

Synthesis of Fe-Co doped MoS_2 nanoflowers

4.0 mmol of $(NH_4)_6Mo_7O_{24}$ and 132 mmol of thiourea were dissolved in 30 mL DI water under vigorous stirring. To this solution, a total of 2.0 mmol of $Fe(NO_3)_3$ and $Co(NO_3)_2$ at various Fe:Co molar compositions (0.2:1.8, 0.5:1.5, 1.0:1.0, 1.5:0.5, 1.8:0.2 mmol) were added. The dopant intake ratio was, therefore, Mo:S:(Co+Fe) = 28:132:7.14. The reaction mixture was further stirred for one hour to form a homogeneous solution. Then, the mixture was transferred into a 50 mL Teflon-lined stainless-steel autoclave and maintained at 180 °C for 24 h. After cooling down to room temperature, the final products were collected by centrifugation, washed thrice with DI water and absolute ethanol, dried at 60 °C for 24 h, and collected for further use. The samples were denoted as Fe_xCo_y-MoS_2 (x:y = 0.10:0.90, 0.25:0.75, 0.50:0.50, 0.75:0.25, 0.90:0.10). The synthesis of Fe-MoS_2 and Co-MoS_2 were the same, except that 2.0 mmol of $Fe(NO_3)_3$ and $Co(NO_3)_2$ were added separately. For undoped MoS_2 synthesis, the same procedure is followed, except for the addition of Fe and Co precursors. To demonstrate the

reproducibility of the MoS_2 synthesis, we compared two MoS_2 batches using two different XRD instruments. The XRD patterns of these two MoS_2 samples are identical; compare Fig. S1 and Fig. S2b.

Synthesis of Fe and Co sulfides

FeS_2 and CoS_2 were synthesized as control samples. 2.0 mmol of $Fe(NO_3)_3$ or $Co(NO_3)_2$ were mixed with 10 mmol of thiourea in 30 mL DI water under vigorous stirring. The reaction mixture was transferred into a 50 mL Teflon-lined stainless-steel autoclave and maintained at 180 ^oC for 24 h. After cooling down to room temperature, the final products were collected by centrifugation, and the post-treatment was done the same as the above procedure.

Characterization Methods

The X-ray diffraction (XRD) pattern was recorded in the 2θ range of 5-80º (step size 0.02º and 5.0 s per step time) by Panalytical X'Pert Pro X-ray powder diffractometer with Cu Kα radiation (λ = 0.154 nm). High-resolution scanning electron microscopy (HR-SEM) images were obtained from a Tescan MAIA3 instrument equipped with an energy dispersive spectrometer (EDS) detector. Samples for transmission electron microscopy (TEM) were prepared by drop-casting well-sonicated solutions containing the nanoparticles in the propanol-water mixture on 300 mesh Cu grids. The samples were allowed to dry overnight at room temperature before analysis. Electron microscopy images and selected area electron diffraction (SAED) patterns were acquired using a Tecnai 12 microscope (FEI) TEM and a JEM 2100, JEOL (200 kV) High-resolution TEM (HR-TEM). The Fe and Co content and the samples' composition were determined by inductively coupled – plasma-optical emission spectrometry (ICP-OES) analysis using Spectro Arcos optical emission spectrometer. XPS data were collected using an X-ray photoelectron spectrometer ESCALAB – 250 ultrahigh vacuum (1 x 10^{-9} bar) apparatus with an Al *K*α X-ray source and a monochromator. The X-ray beam size was 500 μm, survey spectra were recorded with pass energy (PE) of 150 eV, and high energy resolution spectra were recorded with pass energy (PE) of 20 eV. Before XPS analysis, the powder samples were spread on the Indium (In) foil, placed on a sample holder, and sent for analysis. No special preparation was done for all the samples. No Ar-etching was not performed on the sample surfaces. The smart background was subtracted according to AVANTAGE data. The charging effect was corrected by calibrating all the spectra relative to a carbon C 1s peak at 284.8 eV.

Electrode preparation and Electrochemical measurements

Before the electrochemical measurements, the 3 mm glassy carbon (GCE) working electrode (0.071 cm^2 surface) was first polished with 1 μm Al_2O_3 to remove any deposited material, followed by polishing with 0.05 μm Al_2O_3 to make a smooth surface. Then, it was sonicated in water for 30 s using an ultrasonic bath to remove any particles from the surface. A three-electrode cell was used for the electrochemical measurements using an EmStat[3] PalmSens instrument. Impedance measurements were measured using a PalmSens4 potentiostat. A glassy carbon electrode with a diameter of 3 mm was used as the support for the working electrode, with Hg/HgO (KOH, 1.0 M) as the reference electrode and a graphite rod or a platinum wire as the counter electrode. Since Pt wire may dissolve under oxidative conditions and its ions migrate to the working electrode and catalyze the electrochemical reaction, we verified that it does not happen, Fig. S13. The potential mentioned in this work is referenced to the reversible hydrogen electrode (RHE), Eqn. S1.

$$\mathbf{E}\ (vs.\ \text{RHE}) = \mathbf{E}\ (vs.\ \text{Hg/HgO}) + 0.059 * \text{pH} + 0.098\ \text{V} \qquad \text{(S1)}$$

Linear sweep voltammetry (LSV) was recorded at a scan rate of 5 mV s^{-1} in 1.0 M KOH solution (pH ~13.8) as an electrolyte to obtain the polarization curves. During the measurements, the headspace of the cell was continuously purged with Ar at a slow flow rate to prevent atmospheric oxygen from diffusing into the solution. The Tafel slope was calculated from the logarithmic relationship between overpotential and current density based on the LSV curve. Chronoamperometry experiment was performed at a constant overpotential of 390 mV in 1.0 M KOH solution on carbon cloth substrate and further characterized before and after the stability study. Electrochemical impedance spectroscopy measurements were performed at an overpotential of 340 mV from 10 kHz to 0.1 Hz (14 points per decade) with an amplitude of the sinusoidal perturbation fixed at 10 mV. The ECSA measurements were done according to a procedure described elsewhere.[1,2] Cyclic voltammograms scanning in a non-Faradaic region were recorded at different scan rates ranging between 10 to 200 m Vs^{-1} (Fig. S10) to estimate the double-layer capacitance (C_{dl}) by plotting the $\Delta j = (J_a - J_c)$ at 1.025 V (vs. RHE) as a function of the scan rate, where J_a and J_c are the anodic and cathodic current densities, respectively.

Computational methods

All calculations reported in this article were accomplished using plane-wave DFT employing periodic boundary conditions as implemented in the Vienna Ab initio Simulation Package (VASP 5.4.4).[3,4] The generalized gradient approximation Perdew-Burke-Ernzerhof (PBE) functional was used for the exchange-correlation potential.[5] The spin polarization formalism with an energy cutoff of 500 eV for the plane-wave basis was set for all the calculations. Thresholds of 300, 400, and 600 eV were also tested for a selected system to validate that 500 eV was well-off. A 4x4x1 (16 Mo & 32 S atoms) monolayer supercell was used for MoS_2 surface modeling, and a 6x6x1 Monkhorst–Pack k-point grid was applied for the sampling of the Brillouin zone. Calculations at different grid sizes have shown that this number of k-points is enough to derive reproducible results. In calculations, the positions of the ions were relaxed, while the volume and shape of the cell were kept constant. The standard PAW potentials with valence configurations of $4s^2 4p^6 5s^2 4d^4$ for Mo (Mo_sv_GW), $3s^2 3p^4$ for S (S_GW), $4s^2 4p^6 4d^7 5s^1$ for Fe (Fe_sv_GW), $4s^2 4p^6 4d^8 5s^1$ for Co (Co_sv_GW), $2s^2 2p^4$ for O (O_GW_new), and $1s^1$ for H (H_new) were described for electron-ion interactions. The convergence criterion for the self-consistent electronic loop was set to 1×10^{-5} eV, and 0.01 eV/Å was used for the maximum force. For simplicity, in this study, we restricted pH 0. As a first approximation, the solvation effects were neglected, as they are likely to be low in this case. Periodic boundary conditions were applied in all directions, and a 15 Å vacuum was imposed to ensure no significant coupling between periodic slab replicas in the Z-direction. Zero-point energy correction (ZPE) in free energy of all the adsorbates is calculated by assuming an approximation of the quantum harmonic oscillator implemented in the VASP code. The results are collected in Table S5.

To account for the dispersion effect on the optimized geometries, Van der Waals (VDW) corrections were applied based on the DFT-D2 approach proposed by Grimme[6] and implemented in VASP by Bučko.[7] Moreover, we have optimized some selected systems considering both DFT-D2 and DFT-D3 dispersions, while it shows minimal influences, both in terms of geometry and energy (Table S6). Therefore, considering the calculation costs, we maintain the method mentioned above.

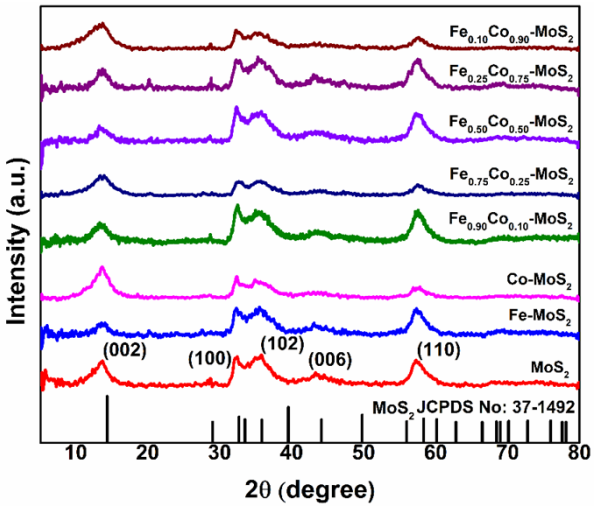

Fig. S1. XRD patterns of 2H-MoS_2, Fe-MoS_2, Co-MoS_2, and Fe_xCo_y-MoS_2 (x,y = 0.10,0.90; 0.25,0.75; 0.50,0.50; 0.75,0.25; 0.90,0.10). Note, for the $Fe_{0.25}Co_{0.75}$-MoS_2, $Fe_{0.50}Co_{0.50}$-MoS_2, and $Fe_{0.90}Co_{0.10}$-MoS_2 additional very minor peak is observed at 28˚ along with some intensity higher than the noise level at around 7˚. These peaks may be attributed to residual from the precursor.

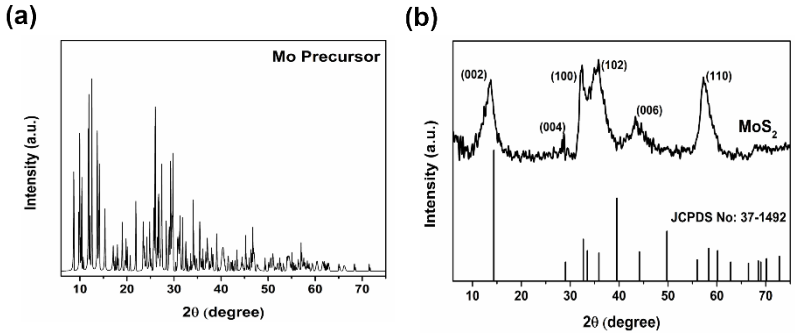

Fig. S2. XRD patterns of (a) Mo precursor ($(NH_4)_6Mo_7O_{24}.4H_2O$), and (b) MoS_2 XRD pattern (using a different instrument) showing the synthesis reproducibility.

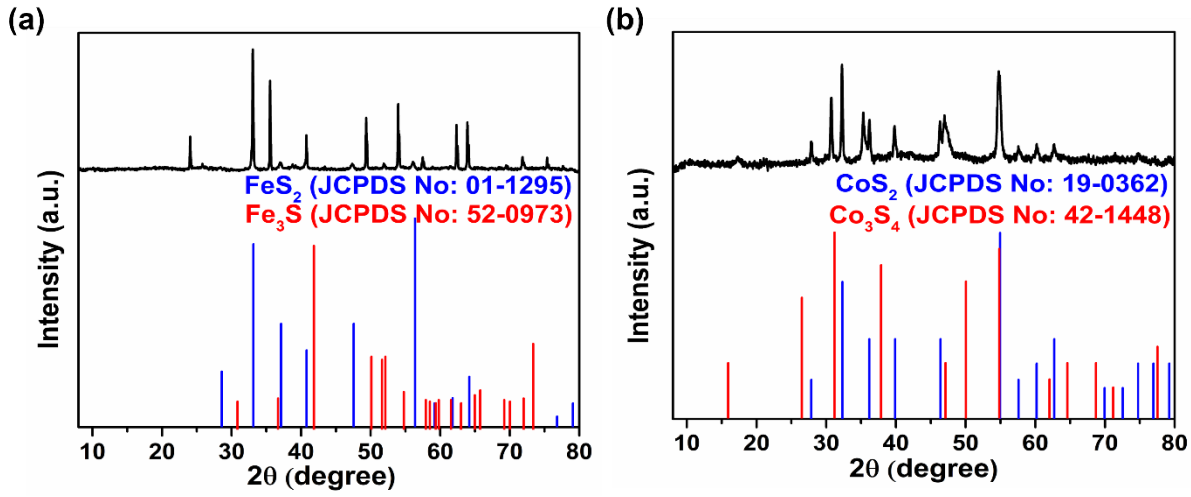

Fig. S3. XRD patterns of synthesized dopant sulfides (a) FeS_2, and (b) CoS_2 catalysts.

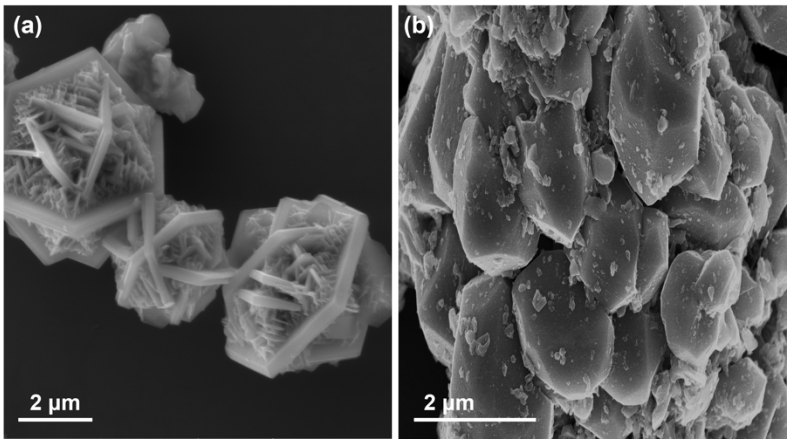

Fig. S4. HR-SEM images of synthesized dopant sulfides (a) CoS_2, and (b) FeS_2.

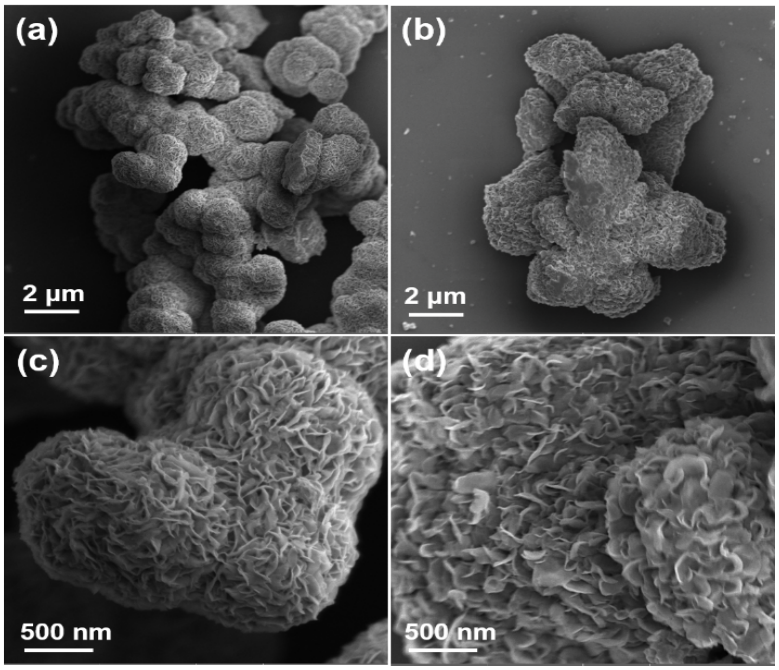

Fig. S5. HR-SEM images of (a, c) Co-MoS_2, and (b, d) Fe-MoS_2.

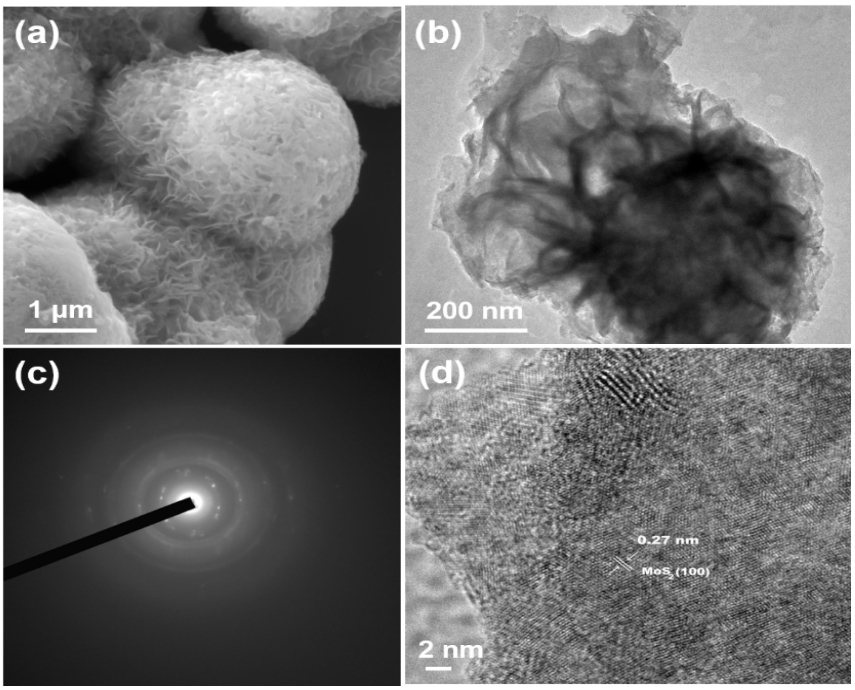

Fig. S6. (a) HR-SEM image of $Fe_{0.10}Co_{0.90}$-MoS_2, (b) TEM image of $Fe_{0.10}Co_{0.90}$-MoS_2 catalyst with low magnification (c) SAED pattern, and (d) High-resolution TEM image of $Fe_{0.10}Co_{0.90}$-MoS_2 catalyst.

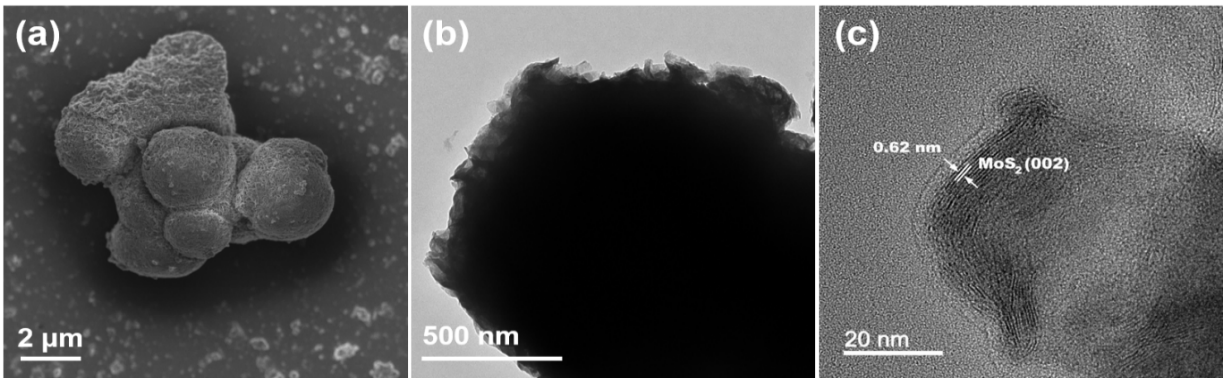

Fig. S7. (a) HR-SEM image, (b) Low magnification TEM image, and (c) High-resolution TEM image of MoS_2.

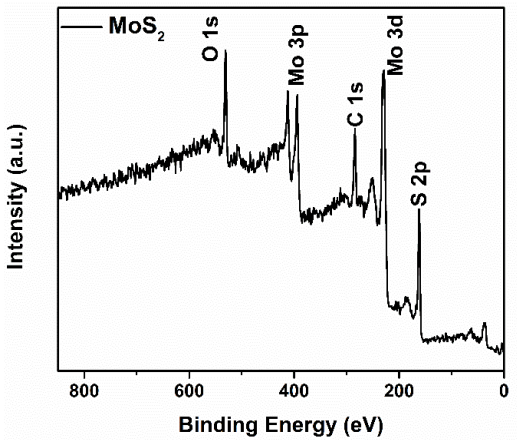

Fig. S8. XPS survey spectrum of MoS_2.

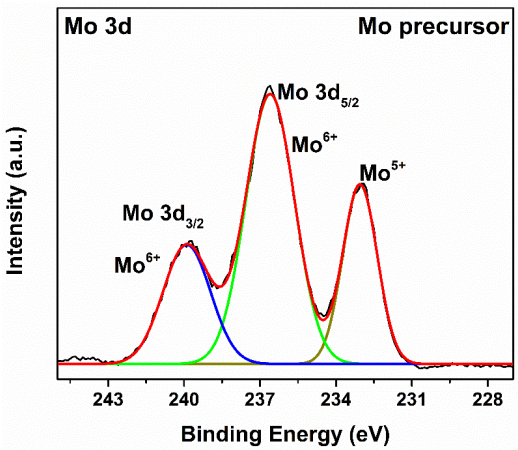

Fig. S9. XPS Mo 3d spectrum of Mo precursor ($(NH_4)_6Mo_7O_{24}).4H_2O$).

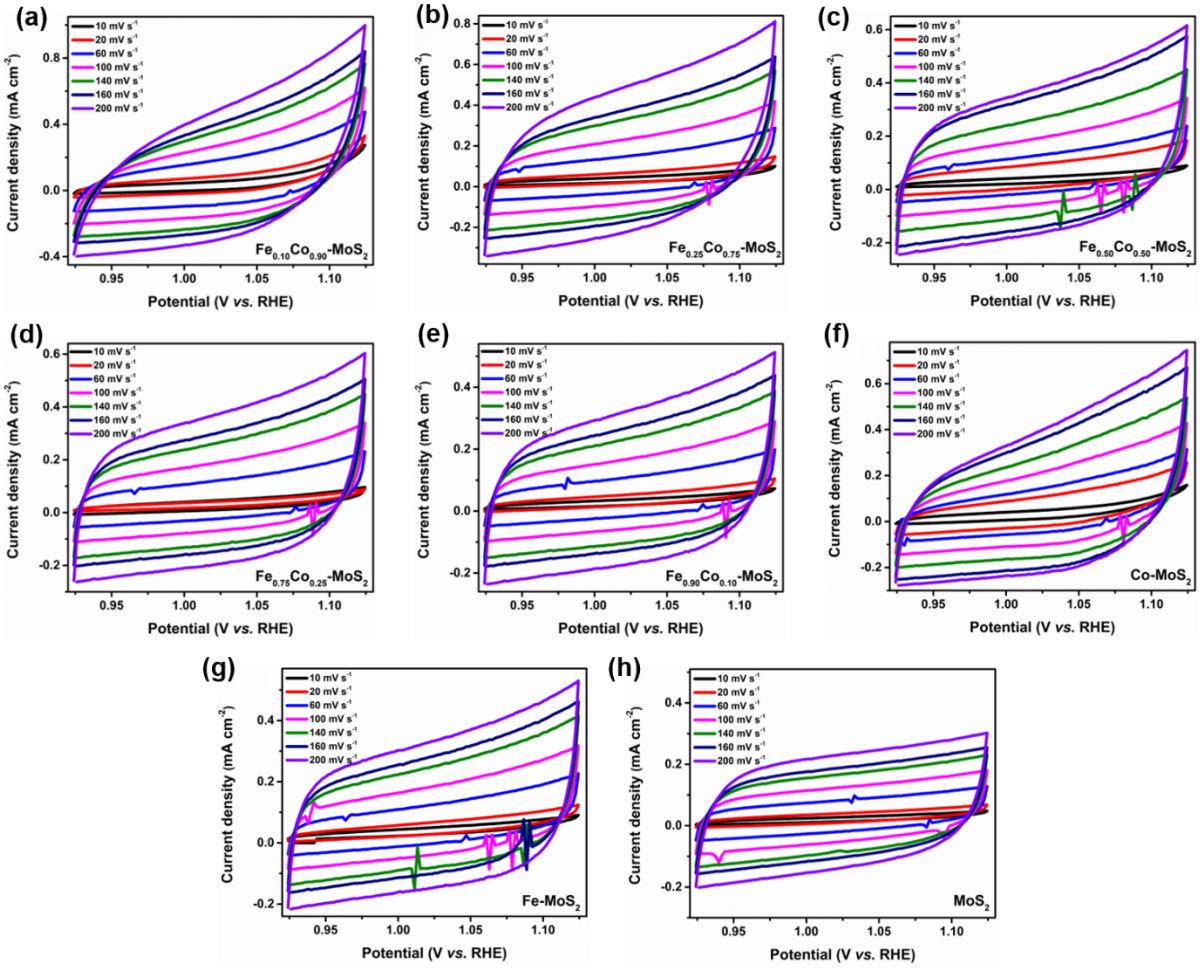

Fig. S10. Cyclic voltammograms of all the catalysts recorded at different scan rates from 10 to 200 mVs^{-1} in 1.0 M KOH solution.

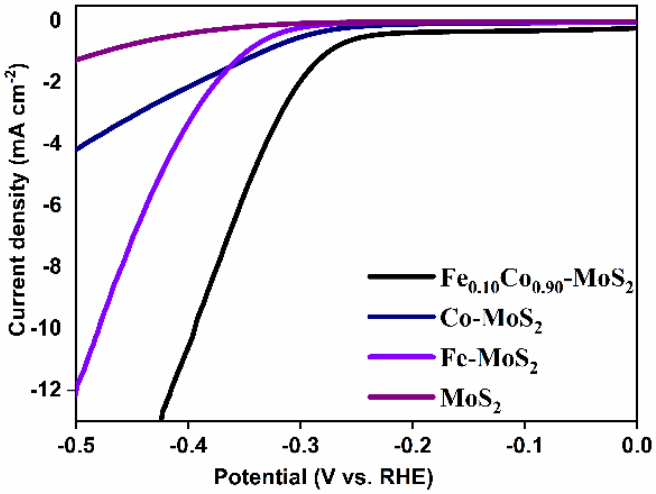

Fig. S11. HER polarization curves performed in 0.5 M H_2SO_4 at a scan rate of 5 mV s^{-1}.

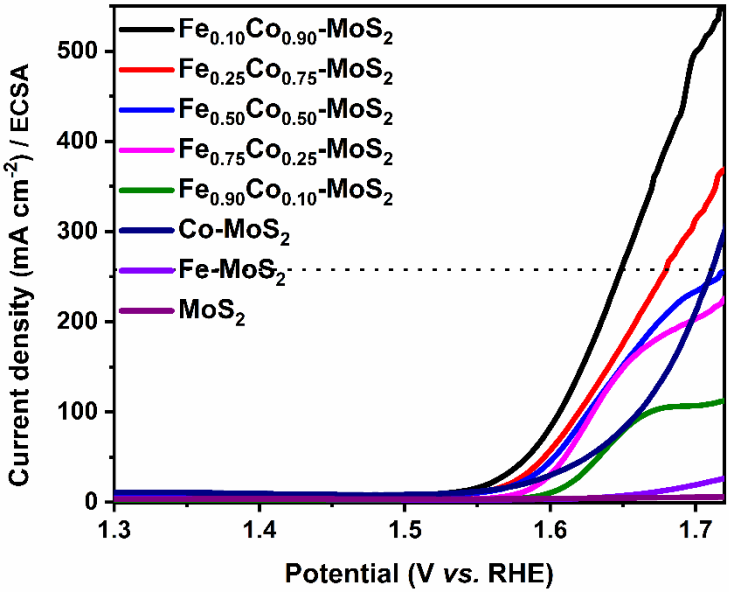

Fig. S12. A plot of LSV curves normalized by the electrochemical active surface area (ECSA).

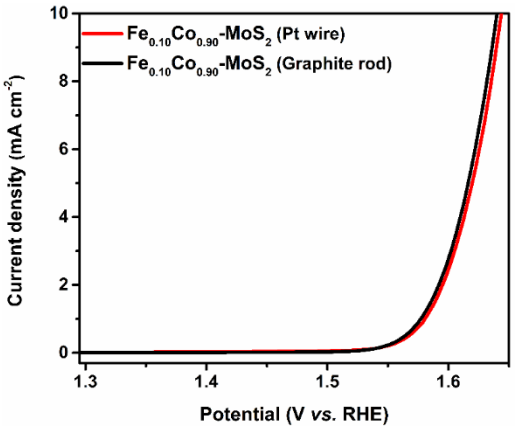

Fig. S13. OER performance of the $Fe_{0.10}Co_{0.90}MoS_2$ catalyst using Graphite electrode and Pt wire as the counter electrode. The scan rate was 5 mV s^{-1}. No change was observed (within the experimental error).

Table S1. Summary of ICP-OES analysis of Fe_xCo_y-$Mo_{1-x-y}S_2$

	Composition (at %)		
Sample	**Fe**	**Co**	**Mo**
MoS_2	-	-	100
Co-MoS_2	0	5.3	94.7
Fe-MoS_2	10.1	0	89.9
$Fe_{0.10}Co_{0.90}$-MoS_2	0.7	4.5	94.8
$Fe_{0.25}Co_{0.75}$-MoS_2	2	4.8	93.2
$Fe_{0.50}Co_{0.50}$-MoS_2	2.6	2.4	95
$Fe_{0.75}Co_{0.25}$-MoS_2	5.5	1.5	93
$Fe_{0.90}Co_{0.10}$-MoS_2	9.9	0.8	89.3

Note: Mo interferes with Co detection resulting in lower concentrations detected for Co.[8]

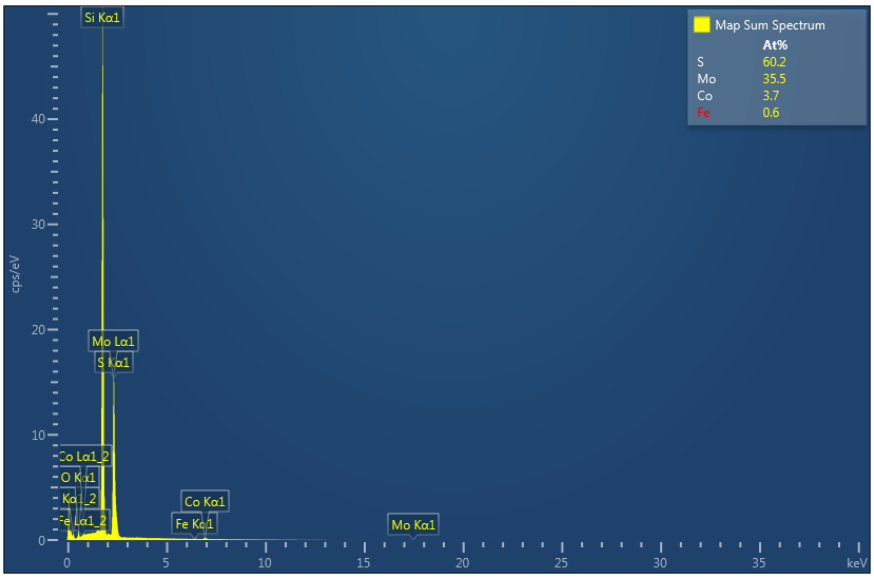

Fig. S14. EDS spectrum of the $Fe_{0.10}Co_{0.90}$-MoS_2 catalyst.

Table S2. Elemental mapping of Mo, S, Co, and Fe as determined by EDS analysis.

	Composition (at %)			
Sample	**Fe**	**Co**	**Mo**	**S**
MoS_2	**-**	**-**	**39.3**	**60.7**
Co-MoS_2	-	7.7	33.8	58.4
Fe-MoS_2	4.4	-	36.8	58.8
$Fe_{0.10}Co_{0.90}$-MoS_2	0.6	3.7	35.5	60.2

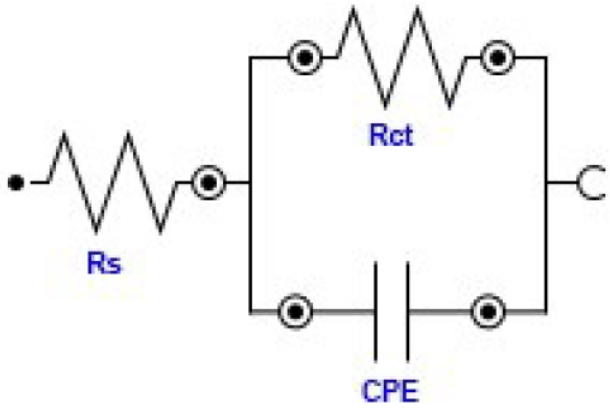

Fig. S15. The equivalent circuit diagram for the EIS.

Table S3. The fitting results of the EIS parameters of various samples.

Sample	Rs (Ω)	Rct (Ω)
MoS_2	10.78	6619
Co-MoS_2	7.83	72
Fe-MoS_2	9.64	1394
$Fe_{0.10}Co_{0.90}$-MoS_2	9.24	24

R_s represents the resistance of the electrolyte.

R_{ct} stands for the charge transfer resistance between catalyst-electrolyte interface, and **CPE** signifies the constant phase element.

Table S4. The atomic % of Mo species as obtained from the XPS deconvoluted spectra.

Catalyst	Area (a.u.)			Species, at%		
	Mo^{+4}	Mo^{+5}	Mo^{+6}	Mo^{+4}	Mo^{+5}	Mo^{+6}
MoS_2	4584	1666	3096	49.0	17.8	13.5
Fe-MoS_2	10421	7112	6891	42.7	29.1	20.9
Co-MoS_2	12433	4950	7899	49.2	19.6	31.2
$Fe_{0.10}Co_{0.90}$-MoS_2	16660	10744	6130	49.7	32	18.3

In order to understand the intrinsic activity of the potent electrocatalyst, we calculated its turnover frequency (TOF), exchange current density, and Faradaic efficiency (FE).

The TOF value was calculated using Eqn. S2.[9]

$$\text{TOF} = \frac{J\,N_A}{4FnECSA} \qquad \text{(S2)}$$

where J is the current density, 4 represents the stoichiometric number of electrons transferred in the OER reaction, ESCA is the electrochemically active surface area of the electrode, F is the Faraday constant (F = 96,485 C mol^{-1}), N_A is the Avogadro's number ($N_A = 6.022 \times 10^{23}$ O_2 molecules/mole), and n is the number of active sites ($n = 1.0 \times 10^{17}/cm^2$) in a flat 1 cm^2 surface of wet-chemistry synthesized MoS_2 sample.[10] The active sites are probably sulfur atoms bound to Co or Fe and not all the Mo sites; hence, the calculated TOF is conservative and is only a lower limit.

The ECSA was calculated from the Cdl value, assuming that the specific capacitance of a flat surface is ~ 40 μF cm^{-2} for 1.0 cm^2 of a real surface area. The ECSA is estimated using the Eqn. S3.

$$\text{ECSA} = \text{Specific capacitance (mF cm}^{-2}\text{)/40 μF cm}^{-2}\text{ per cm}^2 \qquad \text{(S3)}$$

The calculated values for $Fe_{0.10}Co_{0.90}$-MoS_2 are **ECSA: 48 cm^2** and **TOF: 3.25 s^{-1}**.

The exchange current density (ECD) describes the intrinsic charge transfer under equilibrium conditions. A higher exchange current density means a greater charge transfer rate and a lower reaction barrier. The ECD is calculated from the intercept of the X-axis of the Tafel plot Fig 3b. For $Fe_{0.10}Co_{0.90}$-MoS_2, the **ECD** is **1.14×10^{-4}**.

The Faradaic effiency (FE) experiment was performed in a gas-tight H-cell connected to a manometer on the anodic compartment. When a constant potential was applied by chronoamperometry measurement, the change in the water level of the manometer was observed with time. The data recorded are converted into moles of oxygen. The FE was calculated by comparing the amount of oxygen produced by the potentiostatic anodic reaction with the calculated oxygen assuming 100% FE.[11] For $Fe_{0.10}Co_{0.90}$-MoS_2, the **FE** is **~80%.**

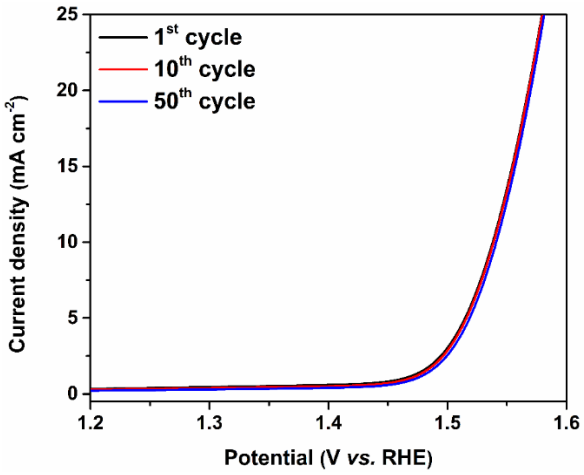

Fig. S16. LSV polarization curves of $Fe_{0.10}Co_{0.90}$-MoS_2 catalyst obtained at different CV cycles.

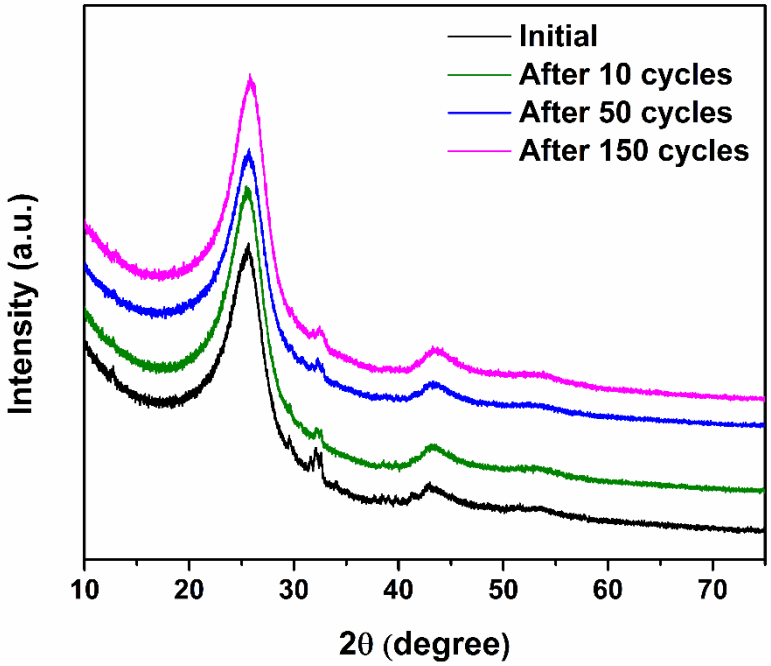

Fig S17. XRD patterns of $Fe_{0.10}Co_{0.90}$-MoS_2 catalyst obtained after different CV cycles. (Note: The peak at 25.6˚ belongs to 'C' from the carbon cloth)

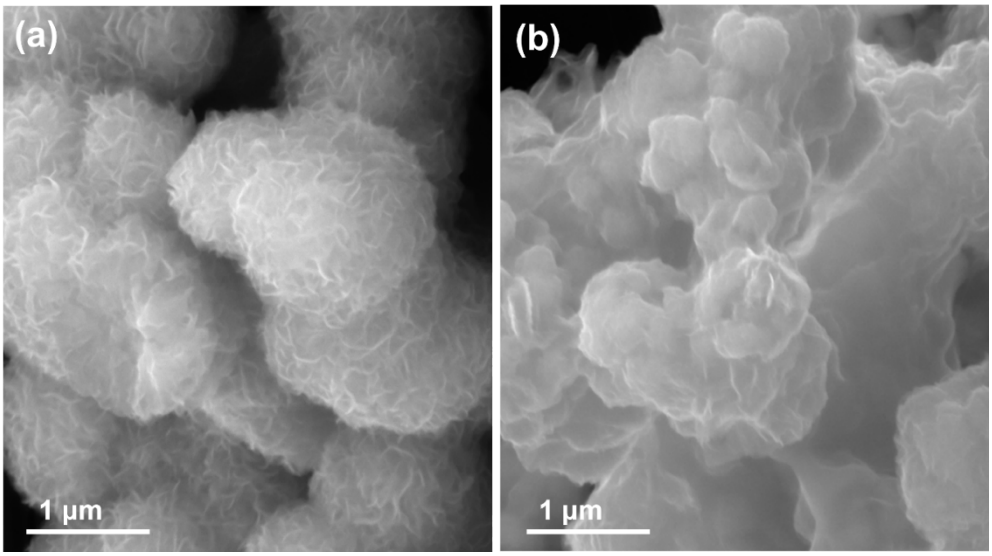

Fig. S18. SEM images of $Fe_{0.10}Co_{0.90}$-MoS_2 catalyst (a) before, and (b) after 1,000 CV cycles.

The XPS characterization was used to investigate the chemical state changes of the catalyst following 1,000 OER electrocatalytic cycles. The XPS survey spectra before and after the electrocatalytic cycles are compared in Fig. S19 and the high-resolution XPS spectra in Fig. S20. All the metals show downshifted binding energies indicating some catalyst oxidation, while no significant change is observed in the sulfur spectrum.

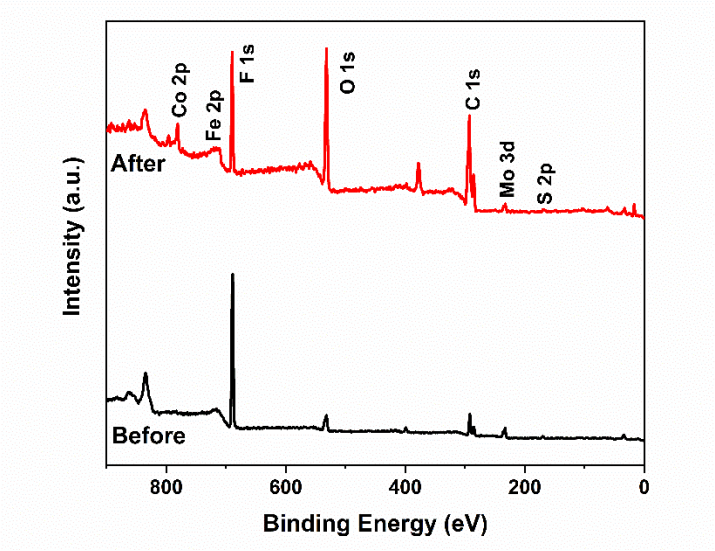

Fig. S19. XPS survey spectra of $Fe_{0.10}Co_{0.90}$-MoS_2 before and after 1,000 CV cycles.

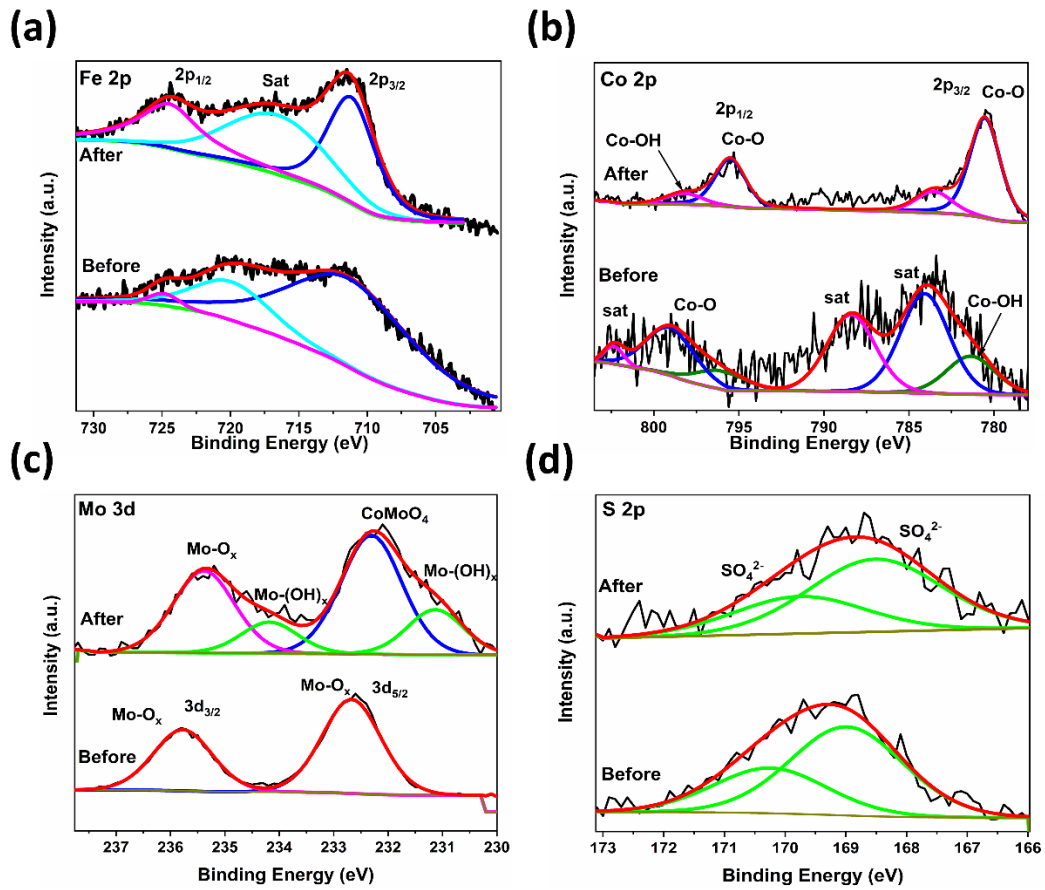

Fig. S20. High-resolution XPS spectra of (a) Fe 2p, (b) Co 2p, (c) Mo 3d, and (d) S 2p of $Fe_{0.10}Co_{0.90}$-MoS_2 before and after 1,000 CV cycles.

Table S5. Summarized ZPE and entropy contributions to Gibbs free energies of steps 1-4.

	ΔG^{exp}_{H2O} [a]	E^{DFT} [b]	ZPE	$T\Delta S^{exp}$ [a]	ZPE-TΔS
H_2O(l)	-2.46(l)	-14.26	0.56	0.216 0.67(0.035 bar)	-0.11
H_2(g)	-	-6.718	0.35	0.403	-0.06
O*	-	-	0.08	0	0.08
*OH	-	-	0.38	0	0.38
*OOH	-	-	0.45	0	0.45

	ΔZPE	TΔS	ΔZPE-TΔ

			S
$H_2O(l) \rightarrow *OH + 1/2H_2$	-0.01	-0.47	0.46
$*OH \rightarrow *O + 1/2H_2$	-0.13	0.21	-0.33
$H_2O(l) + O* \rightarrow *OOH + 1/2H_2$	-0.02	-0.47	0.45
$*OOH \rightarrow * + O_2 + 1/2H_2$	0.17	0.73	-0.56

[a] Experimental Gibbs free formation energies and entropic contributions at standard conditions: T = 298 K and P = 1 bar as listed in the CRC Handbook.[12]
[b] The calculated DFT total energies are for a single molecule in the gas phase.[13]

Table S6. Gibbs free energy changes (in eV) at different optimization methods.

Method	*	***OH**	***O**	***OOH**	* + O_2
Opt[a]	0	0.55	0.82	3.75	4.92
opt_sp[b]	0	0.46	0.75	3.6	4.92
opt_D2[c]	0	0.46	0.74	3.6	4.92
opt_D3[d]	0	0.45	0.77	3.6	4.92

[a]Optimization of the intermediates without dispersion correction
[b]Addition of D2-dispersion correction in single points on the optimized geometries
[c]Optimization of the intermediates with D2-dispersion correction
[d]Optimization of the intermediates with D3-dispersion correction

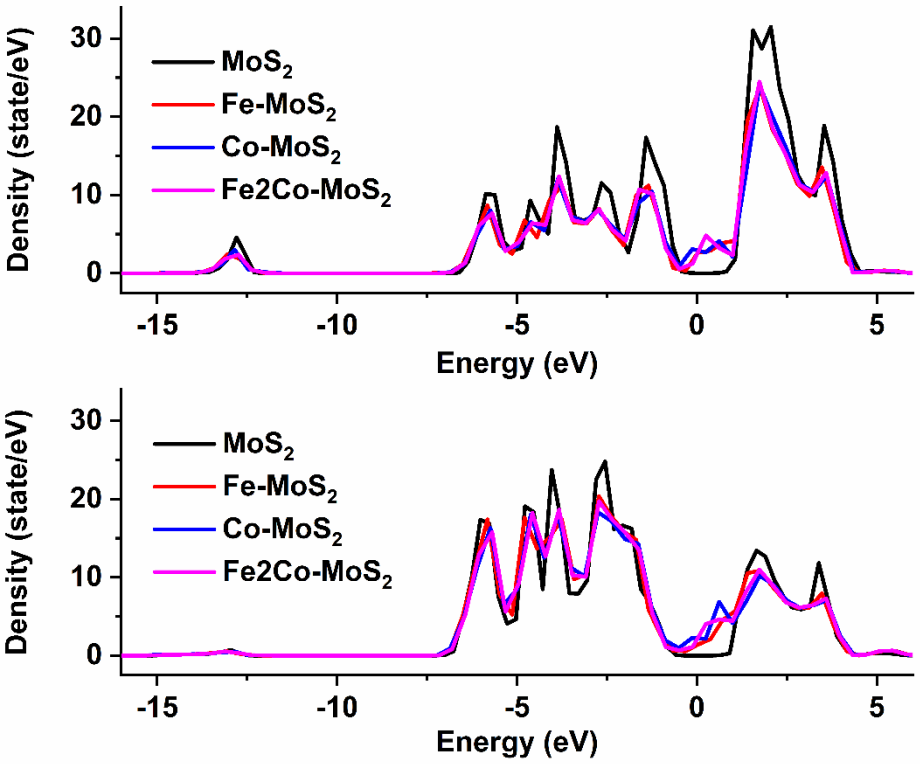

Fig. S21. Upper panel: PDOS plot for d-orbitals of Mo, lower panel: PDOS plot for p orbitals of S.

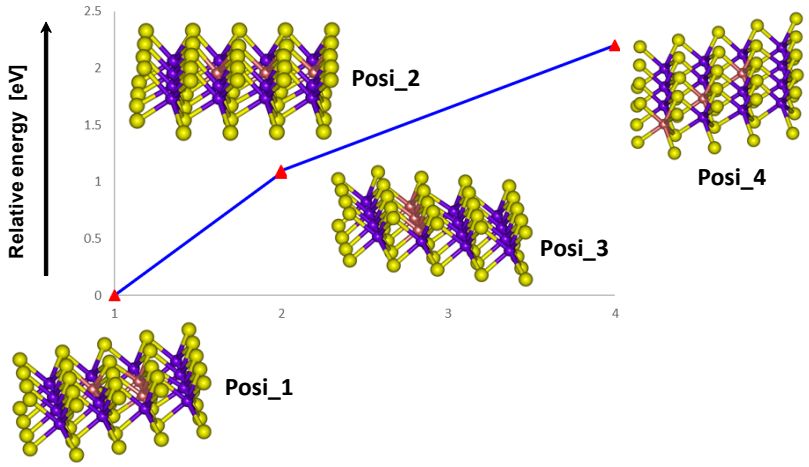

Fig. S22. The calculated relative energies (in eV) of the Fe-doped MoS_2 surface (3Fe- MoS_2) in the four possible arrangements. The purple, yellow, and brown spheres stand for Mo, S, and Fe atoms.

Table S7. Comparison of OER performance in alkaline media for $Fe_{0.10}Co_{0.90}$-MoS_2 catalyst with other non-noble metal electrocatalysts.

Catalyst	Support/ Electrode	Electrolyte	Tafel slope [mV dec^{-1}]	η_{10} [mV] [a]	Reference
Co_3O_4@CoO SC	RDE	1 M KOH	89	430	14
NPCN/CoNi-NCNT	GCE	0.1 M KOH	165	360	15
NiCo/PFC	RDE	0.1 M KOH	106	400	16
FeCo@NG/NCNT	GCE	1 M KOH	77	450	17
CoP/CoP_2@NPCN Ts	Carbon paper	1 M KOH	50	300	18
FeCo@NC	RDE	1 M KOH	50.19	270	19
MoS_2@$Ni(OH)_2$/NF	Ni Foam	1 M KOH	49	233	20
NCF-MOF	GCE	0.1 M KOH	49	320	21
$Fe_{0.25}$-CoMoCH/NF	Ni Foam	1 M KOH	46	232	22
MSQDs-AC	GCE	1 M KOH	39	370	23
Co_9S_8@MoS_2	GCE	1 M KOH	61	430	24
MoS_2/Co-N-CN_2-900°C	GCE	1 M KOH	169	442	25
Co_3S_4@MoS_2	GCE	1 M KOH	88	330	26
Co,Nb-MoS_2/ TiO_2 HSs	Ni Foam	1 M KOH	65	260	27
Co,Nb-MoS_2 NSs	Ni Foam	1 M KOH	147.6	320	27
MoS_2/CoB-Se/CC	Carbon Cloth	1 M KOH	86	270	28
CoS-doped βCo$(OH)_2$@MoS_{2+x}	GCE	1 M KOH	68	380	29
CoA@CNC- 700	RDE	0.1 M KOH	-	460	30
Co_3O_4–MoS_2	Ni Foam	1 M KOH	46	298	31
Ni_3S_2@MoS_2/FeOOH	Ni Foam	1 M KOH	49	234	32
MoS_2-NiS_2/NGF	Ni Foam	1 M KOH	-	370	33
$Fe_{0.10}Co_{0.90}$-MoS_2	GCE	1 M KOH	78	380	**This work**

[a]represents the overpotential (η) current density of 10 mA cm^{-2} vs. RHE.

*RDE- Rotating Disk Electrode, GCE- Glassy Carbon Electrode. Note that our result is comparable to or better than other works on GCE or RDE; other supports show better activities due to the support properties.

References

1 C. C. L. McCrory, S. Jung, J. C. Peters and T. F. Jaramillo, *J Am Chem Soc*, 2013, **135**, 16977–16987.

2 V. Kuraganti, A. Jain, R. Bar-Ziv, A. Ramasubramaniam and M. Bar-Sadan, *ACS Appl Mater Interfaces*, 2019, **11**, 25155–25162.

3 G. Kresse and J. Furthmüller, *Phys Rev B*, 1996, **54**, 11169–11186.

4 J. Hafner, *J Comput Chem*, 2008, **29**, 2044–2078.

5 J. P. Perdew, K. Burke and M. Ernzerhof, *Phys Rev Lett*, 1996, **77**, 3865.

6 S. Grimme, J. Antony, S. Ehrlich and H. Krieg, *J Chem Phys*, 2010, **132**, 154104..

7 T. Bucko, J. Hafner, S. Lebegue and J. G. Angyán, *J Phys Chem A*, 2010, **114**, 11814–11824.

8 L. Nenni and M. Amara, *Anal chem Indian j*, 2012, **11**, 282–288.

9 J. Benson, M. Li, S. Wang, P. Wang and P. Papakonstantinou, *ACS Appl Mater Interfaces*, 2015, **7**, 14113–14122.

10 J. Kibsgaard, T. F. Jaramillo and F. Besenbacher, *Nat Chem*, 2014, **6**, 248–253.

11 R. Liu, S. Gu, H. Du and C. M. Li, *J Mater Chem A*, 2014, **2**, 17263–17267.

12 Lide D. R., *Handbook of Chemistry and Physics*, 83rd edn., 2002.

13 M. Bajdich, M. García-Mota, A. Vojvodic, J. K. Nørskov and A. T. Bell, *J Am Chem Soc*, 2013, **135**, 13521–13530.

14 C.-W. Tung, Y.-Y. Hsu, Y.-P. Shen, Y. Zheng, T.-S. Chan, H.-S. Sheu, Y.-C. Cheng and H. M. Chen, *Nat Commun*, 2015, **6**, 8106.

15 Y. Hou, S. Cui, Z. Wen, X. Guo, X. Feng and J. Chen, *Small*, 2015, **11**, 5940–5948.

16 G. Fu, Y. Chen, Z. Cui, Y. Li, W. Zhou, S. Xin, Y. Tang and J. B. Goodenough, *Nano Lett*, 2016, **16**, 6516–6522.

17 B. Du, Q.-T. Meng, J.-Q. Sha and J.-S. Li, *New J Chem*, 2018, **42**, 3409–3414.

18 H. Li, S.-M. Xu, H. Yan, L. Yang and S. Xu, *Small*, 2018, **14**, 1800367.

19 M. Li, T. Liu, X. Bo, M. Zhou and L. Guo, *J Mater Chem A*, 2017, **5**, 5413–5425.

20 C. Wei, C. Liu, L. Gao, Y. Sun, Q. Liu, X. Zhang and J. Guo, *J Alloys Compd*, 2019, **796**, 86–92.

21 W. Ahn, M. G. Park, D. U. Lee, M. H. Seo, G. Jiang, Z. P. Cano, F. M. Hassan and Z. Chen, *Adv Funct Mater*, 2018, **28**, 1802129.

22 M. Cai, X. Lu, Z. Zou, K. Guo, P. Xi and C. Xu, *ACS Sustain Chem Eng*, 2019, **7**, 6161–6169.

23 B. Mohanty, M. Ghorbani-Asl, S. Kretschmer, A. Ghosh, P. Guha, S. K. Panda, B. Jena, A. V. Krasheninnikov and B. K. Jena, *ACS Catal*, 2018, **8**, 1683–1689.

24 H. Zhu, J. Zhang, R. Yanzhang, M. Du, Q. Wang, G. Gao, J. Wu, G. Wu, M. Zhang, B. Liu, J. Yao and X. Zhang, *Adv Mater*, 2015, **27**, 4752–4759.

25 X. Hou, H. Zhou, M. Zhao, Y. Cai and Q. Wei, *ACS Sustain Chem Eng*, 2020, **8**, 5724–5733.

26 Y. Guo, J. Tang, H. Qian, Z. Wang and Y. Yamauchi, *Chem Mater*, 2017, **29**, 5566–5573.

27 D. C. Nguyen, T. L. Luyen Doan, S. Prabhakaran, D. T. Tran, D. H. Kim, J. H. Lee and N. H. Kim, *Nano Energy*, 2021, **82**, 105750.

28 M. Song, Y. Zhao, Z. Wu and X. Liu, *Sustain Energy Fuels*, 2020, **4**, 5036–5041.

29 T. Yoon and K. S. Kim, *Adv Funct Mater*, 2016, **26**, 7386–7393.

30 M. Shen, K. Gao, F. Xiang, B. Wang, L. Dai, L. Zheng, F. Baker, C. Duan, Y. Zhang, S. Sun and Y. Ni, *J Power Sources*, 2020, **450**, 227640.

31 A. G. Abd-Elrahim and D.-M. Chun, *J Alloys Compd*, 2021, **853**, 156946.

32 M. Zheng, K. Guo, W.-J. Jiang, T. Tang, X. Wang, P. Zhou, J. Du, Y. Zhao, C. Xu and J.-S. Hu, *Appl Catal B Environ*, 2019, **244**, 1004–1012.

33 P. Kuang, M. He, H. Zou, J. Yu and K. Fan, *Appl Catal B Environ*, 2019, **254**, 15–25.